Experimental Mechanics (2022) 62:1227–1240
https://doi.org/10.1007/s11340-022-00874-2

RESEARCH PAPER

Impact Compression Test of Ice by Combining SHPB Method and High-Speed Camera Observation

Y. Nakao[1] · H. Yamada[2] · N. Ogasawara[2] · T. Matsuzawa[3]

Received: 1 April 2022 / Accepted: 1 June 2022 / Published online: 8 July 2022

Abstract

Background It is difficult to achieve stress equilibrium at both ends of the specimen of brittle materials such as ice because cracks are generated during impact compression.

Objective The present study investigated the compressive stress of pure ice at − 10 °C by using the split Hopkinson pressure bar (SHPB) method.

Methods An SHPB compression test using flanged bars was conducted on pure ice specimens while simultaneously observing their internal deformation and fracture state by using a high-speed camera. The results were analyzed defining that dynamic equilibrium was established when the stress error rate between both ends of the specimen was within ± 15%.

Results The results demonstrated that establishing the dynamic equilibrium and contact condition between specimen and testing apparatus are crucial for performing the SHPB compression test on ice. They also showed a correlation between crack generation/propagation and stress rate variation and that the fracture stress at strain rates > 10^2 s^{-1} can be defined; therefore, the fracture stress measured at strain rates of approximately 10^1–10^3 s^{-1} exhibited a positive strain rate dependence.

Conclusions The fracture behavior and stress of ice at high strain rates can be determined by combining the SHPB method with high-speed camera observation.

Keywords Ice · split Hopkinson pressure bar · Compression · Strain rate · Fracture · High-speed camera observation

Introduction

The split Hopkinson pressure bar (SHPB) method proposed by Kolsky [1, 2] is the most famous impact test to measure the deformation of materials under high strain rates. An SHPB compression apparatus typically consists of three long bars: a striker, an input bar, and an output bar. The specimen is sandwiched between the input and output bars. Under this condition, when the striker ejected by air pressure or other means impacts the input bar, an elastic stress wave propagates in the latter and reaches the specimen as an incident wave. Then, some of this wave deforms the specimen and propagates along the output bar, while the rest is reflected at the specimen/input bar interface and propagates back in the input bar as a reflected wave. The stress and strain acting on the specimen, including the strain rate, can be calculated by measuring these elastic stress waves propagating in the bars and applying the one-dimensional elastic wave theory [3]. Since, in principle, this test can be conducted on various specimens, its application has been recently developed for not only metallic [4, 5] but also non-metallic materials [6, 7], which are mainly ductile. Moreover, the stress–strain relationship can be derived by confirming the equilibrium of the stresses applied at both ends of the specimen (hereafter called dynamic equilibrium). On the other hand, it is difficult to achieve stress equilibrium at both ends of the specimen since brittle materials can fracture even at small strains. Therefore, some techniques such as controlling the incident wave have been reported for applying the SHPB method to brittle materials [8, 9].

✉ H. Yamada
ymda@nda.ac.jp

[1] Graduate School of Science and Engineering, National Defense Academy, 1-10-20, Hashirimizu, Yokosuka, Kanagawa 239-8686, Japan

[2] Department of Mechanical Engineering, National Defense Academy, 1-10-20, Hashirimizu, Yokosuka, Kanagawa 239-8686, Japan

[3] National Maritime Research Institute, 6-38-1, Shinkawa, Mitaka 181-0004 Tokyo, Japan

In the present study, we focused on the application of the SHPB method to ice, which is a well-known brittle material. Ice exhibits ductile or brittle behavior depending on the strain rate, that is, it undergoes brittle fracture at high strain rates [10–12]. The impact fracture of ice has become an important issue in various fields; examples include countermeasures against hail damage to cars, houses, and aircraft, and protection against ice debris impacting space rockets during launch. It is also key in improving the icebreaker technology for resource exploitation in the Arctic, Antarctic, and other cold regions.

The mechanical properties of ice have been widely investigated, generally through compression and tensile tests. Previous studies have shown that the ice compressive stress depends on various parameters, such as temperature [13, 14], strain rate [15, 16], and ice crystal structure [17]. In this work, we focused mainly on the strain rate dependence, which is significant as regards the compressive stress of ice. According to previous studies, the maximum compressive stress of the ice, which primarily indicates fracture stress, increases along with the strain rate up to ~ 10^{-3} s^{-1}, and uniaxial compression tests at − 10 °C have demonstrated that ductile–brittle transition occurs at strain rates of the order of 10^{-3} s^{-1} [10]. In the brittle region, Schulson [18] reported that the maximum compressive stress decreases from 10 to 6 MPa when increasing the strain rate from 10^{-3} to 10^{-1} s^{-1}, while Cole [19] suggested that the maximum compressive stress is independent of the strain rate in the range of 10^{-2}–10^{-1} s^{-1}. Besides, Jones [20] observed an increase in maximum compressive stress when incrementing the strain rate from 10^{-1} to 10^{1} s^{-1}.

Although there are relatively few studies on the impact strain rate, SHPB experiments have been conducted recently. Dutta et al. [21, 22] showed that at high strain rates of 10^{2} to 10^{3} s^{-1}, at − 10 °C and − 40 °C, the ice maximum compressive stress is almost the same as that in the quasi-static deformation regime. Kim and Keune [23] reported a maximum compressive stress nearly constant in the strain rate range of 400–2600 s^{-1}, with an average value of 19.7 MPa at 0 °C. Shazly et al. [24, 25] observed a positive strain rate dependence of the maximum compressive stress of ice in the strain rate range of 60–1400 s^{-1} at − 10 °C and − 30 °C. Further, they reported that the ice strength is greatly influenced by the test temperature, while the effect of the specimen end constraint by the input and output bars is negligible [24, 25]. Furthermore, referring to the quasi-static test results of Schulson et al. [17], the ice strength continues to increase when raising the strain rate from 0.01 to 1400 s^{-1} [24, 25]. Song et al. [28] recently reported an increase in compressive strength along with the strain rate in the 500–1200 s^{-1} range. The SHB method should confirm whether stress equilibrium is established at both ends of the specimen; although it was mentioned in some of these previous studies, it was not shown in the figures in most of them; thus, a third party cannot verify that dynamic equilibrium had been actually established in the reported cases.

In the SHPB method, the stress–strain relationship can be calculated in the following three ways when the material and cross-sectional area of the input and output bars are the same:

(i) (when using an incident wave, a reflected wave, and a transmitted wave)

$$\sigma(t) = \frac{AE}{2A_S}\left[\varepsilon_I(t) + \varepsilon_R(t) + \varepsilon_T(t)\right] \tag{1}$$

$$\dot{\varepsilon}(t) = \frac{C_0}{L_S}\left[\varepsilon_I(t) - \varepsilon_R(t) - \varepsilon_T(t)\right] \tag{2}$$

$$\varepsilon(t) = \frac{C_0}{L_S}\int_0^t \left[\varepsilon_I(t) - \varepsilon_R(t) - \varepsilon_T(t)\right]dt \tag{3}$$

(ii) (when using an incident wave and a reflected wave)

$$\sigma(t) = \frac{AE}{A_S}\left[\varepsilon_I(t) + \varepsilon_R(t)\right] \tag{4}$$

$$\dot{\varepsilon}(t) = \frac{2C_0}{L_S}\varepsilon_R(t) \tag{5}$$

$$\varepsilon(t) = \frac{2C_0}{L_S}\int_0^t \varepsilon_R(t)dt \tag{6}$$

(iii) (when using an incident wave and a transmitted wave)

$$\sigma(t) = \frac{AE}{A_S}\varepsilon_T(t) \tag{7}$$

$$\dot{\varepsilon}(t) = \frac{2C_0}{L_S}\left[\varepsilon_I(t) - \varepsilon_T(t)\right] \tag{8}$$

$$\varepsilon(t) = \frac{2C_0}{L_S}\int_0^t \left[\varepsilon_I(t) - \varepsilon_T(t)\right]dt \tag{9}$$

where A_S and L_S are the cross-sectional area and length of the specimen, respectively, A, E, and C_0 are the cross-sectional area, elastic modulus, and elastic wave velocity of the input and output bars, correspondingly, and,$\varepsilon_I(t)$ $\varepsilon_R(t)$, and $\varepsilon_T(t)$ are the strain values of the incident, reflected, and transmitted waves, respectively. In (i), the incident, reflected, and transmitted waves were used to derive the average nominal values of stress, strain, and strain rate, based on the one-dimensional elastic wave theory. Besides, the following condition is required for achieving a dynamic equilibrium:

$$\varepsilon_I(t) + \varepsilon_R(t) = \varepsilon_T(t) \tag{10}$$

Therefore, if the dynamic equilibrium is established, equations (1)–(3) can be expressed as equations (4)–(6) and (7)–(9). When the SHPB method is applied to metallic materials, equations (7)–(9), which use only incident and transmitted waves, are often utilized after confirming the dynamic equilibrium. This is because, compared with the incident and transmitted waves, the reflected wave is more susceptible to disturbance factors, which influence the stress–strain relationship of the specimen when this wave is used.

Table 1 summarizes the previous studies that conducted SHPB compression tests on ice [21–29]. Most of them used equations (1)–(3) to calculate the stress–strain relationship. However, it is questionable whether it is correct to use the average nominal values of stress, strain rate, and strain to evaluate the compressive property of brittle materials such as the ice that fracture via crack propagation. This is because the impact tests on ice require larger specimens than those on metallic materials, and the conditions make it difficult to establish stress equilibrium due to crack propagation. When the specimen is small, the stress equilibrium can be assumed as confirmed with little effect, considering the measurement resolution. However, it is unclear whether the same quasi-static test conditions could be achieved for smaller specimens in impact tests since the crystal grain size of ice is relatively large; moreover, if the stress difference between both ends of the specimen is extremely large, averaging is meaningless. Therefore, a combination with other evaluation methods is necessary, for example, to visualize the deformation state simultaneously with the SHPB test. Digital image correlation (DIC) has been recently utilized to quantitatively visualize the deformation state [30]. In this technique, random patterns applied to a specimen by spraying or other means can be tracked via image processing to analyze displacement and strain; however, the application of random patterns to ice is tricky. On the other hand, since ice is a transparent material, its inner cracks can be observed by photographing the deformation process with a high-speed camera. In previous studies, Shazly et al. [24, 25] and Song et al. [28] have attempted to observe the ice fracture using a high-speed camera. However, they did not clearly observe crack generation/propagation, and the relationship between compressive stress and fracture behavior of ice has not been adequately discussed.

The purpose of this study is to properly evaluate the compressive stress and fracture behavior of ice through the SHPB method. Therefore, we constructed an apparatus that combines an SHPB method with a cooling chamber and conducted the experiments at − 10 °C, while simultaneously observing with a high-speed camera the state of the cracks inside the ice specimen during impact deformation; the relationship between the cracks and the stress at the two specimen ends was also investigated. Furthermore, the compressive stress of the ice and its fracture behavior were investigated by changing test conditions such as the contact conditions between input/output bars and specimen and the specimen length.

Experimental Procedure

Specimen Preparation

To not vary the test conditions, this study was conducted on specimens of the same commercially available pure ice used in previous quasi-static tests [31]. Rectangular parallelepipeds with a size of 20 mm × 20 mm × 30 mm were cut out from a pure ice block (260 mm × 550 mm × 1000 mm) using a band saw and stored in a − 20 °C freezer. The bottom surface of each rectangular parallelepiped ice taken out of the freezer was slightly melted on a metal plate and adhered to a flange pre-cooled with dry ice; this flange was made of AA2017 aluminum alloy because of its good thermal conductivity. Then, the upper surface of the ice was cut with a microtome (REM-710, Yamato Kohki Industrial Co., Ltd) in 10 μm steps to obtain a flat surface, and a total of 173 specimens with different heights (*Ls*; 5, 10, 20, and 25 mm) were prepared. The specimens with a *Ls* of 5 and 10 mm were used for the experiments with strain rate range

Table 1 Previous studies that use the split Hopkinson pressure bar method

Researchers	Calculation formula	Reference to stress/force equilibrium	Graphical display of stress/force equilibrium	High-speed camera observation
Dutta et al. [21, 22]	(1) – (3)	×	×	×
Kim and Keune [23]	(1) – (3)	×	×	×
Shazly et al. [24, 25]	(7), (5), (6)	○	×	△
Wu and Prakash [26]	(7), (5), (6)	○	×	×
Bragov et al. [27]	No description	×	×	×
Song et al. [28]	(1) – (3)	○	×	△
Potter et al. [29]	No description	○	○	×

of 10^2–10^3 s^{-1}, while the tests at ~ 10^1 s^{-1} were conducted on those having a *L*s of 20 and 25 mm.

Experimental Apparatus

Experimental setup

Figure 1 schematizes the SHPB testing apparatus used in this study. Given the low strength of the ice, bars with a cross-sectional area as small as possible and a low elastic modulus should be used for high measurement sensitivity. However, aluminum alloys with a low elastic modulus have high thermal conductivity, which may affect the sensitivity of the strain gauges at low temperatures. Therefore, each bar was made of stainless steel (ISO 4301–304-00-I), which has relatively low thermal conductivity and is resistant to rust. In general, the SHPB testing apparatus is designed so that the diagonal length of the specimen bottom does not exceed the diameters of the input and output bars; for example, if the specimen bottom is a square with a side length of 20 mm, bars with a diameter of ≥ 29 mm must be used. However, increasing the bar diameter results in poor measurement sensitivity. Therefore, we set the diameter of the input and output bars to 16 mm. Furthermore, aluminum alloy flanges with a diameter of 34 mm and a thickness of 4.5 mm, and of the same type as that used for flattening the ice surface when preparing the specimens, were screwed to the tip of these bars; the use of an aluminum alloy only for the flanges allowed cooling only around the specimen while avoiding excessive cooling of the strain gauges. Tateyama et al. [32, 33] have conducted SHPB tests with flanged bars on foamed films, reporting that the stress equilibrium was established at both ends of the specimen even with flanges and the axial stress could be measured with high sensitivity.

As shown in Fig. 2(a), the SHPB testing apparatus was combined with a cooling chamber, which has been used in our previous study [31]. The specimen was placed between the flanges (Fig. 2(b)). The flange with the ice specimen was attached to the output bar side, and two methods were used to compare the effect of the contact condition between flanges and specimen. In one case, the flange on the input bar side did not adhere to the ice specimen but was contacted by applying a small load with restoring force of a rubber attached to the bar (only the output bar side was directly bonded to a flange). In the other, the top surface of the specimen was slightly melted and then adhered to the pre-cooled flange on the input bar side so that both the specimen ends were firmly contacted to the flanges. In each experiment, the dimensions of the specimens were measured before installing the specimens in the chamber.

To record the deformation and fracture of the ice specimens, a high-speed camera (ULTRA Cam HS-106E, nac Image Technology Inc.) was installed in front of the observation window of the cooling chamber. The images were taken at a frame rate of 500,000 fps, a pixel count of 360 × 410 pixels, and a shutter speed of 0.2 μs; the image resolution derived from the shooting conditions was 74 μm. A strobe (PE-60SG, Panasonic Photo & Lighting Co., Ltd.) was used as the light source, and the specimens were illuminated from the opposite side of the camera, as shown in Fig. 1. By using a strobe emitting light instantaneously, the ice specimens were not affected by heat. To accommodate observation of the cracks inside the ice specimens, the chamber window was made of high-performance glass with a transmitted wavefront aberration of λ/8 (λ = 632.8 nm); furthermore, the nitrogen gas used for cooling was reused and sprayed on this glass window to prevent moisture condensation while allowing observation of the inside.

The strain gauges were mounted to the input and output bars to measure the propagating elastic stress waves. Their output was passed through a Wheatstone bridge circuit and a differential amplifier (5307, NF Corporation) which eliminate high-frequency electrical noise via an 1-MHz filter, and recorded on a digital oscilloscope (DL850E, Yokogawa Test & Measurement Corporation) with a sampling period of 1 MHz. The launch air pressure of the striker was varied between 0.025 and 0.4 MPa to obtain strain rates ranging from ~ 10^1 to 10^3 s^{-1}.

In the SHPB method, oscillations of strain wave are likely to occur when the rise of the incident wave is steep. Therefore, many impact tests utilize a buffer material as a pulse shaper on the contact surface between striker and input bar, which slows down the rise of the strain wave [8, 9]; this allows the generation of strain waves with less turbulence. Figure 3 compares incident waves obtained with and without using a 0.27-mm-thick cardboard piece as the pulse shaper. Without the pulse

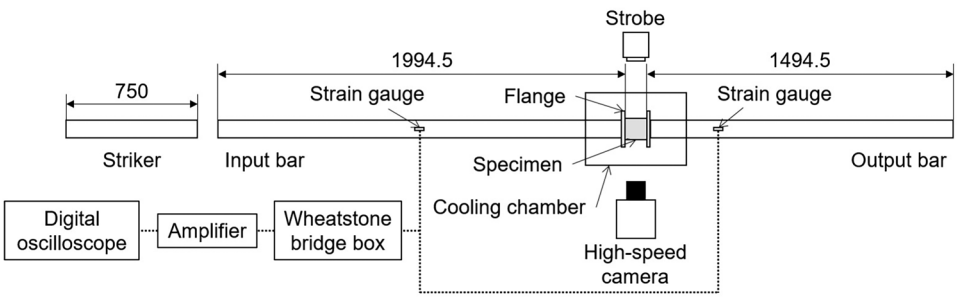

Fig. 1 Schematic of the split Hopkinson pressure bar testing apparatus

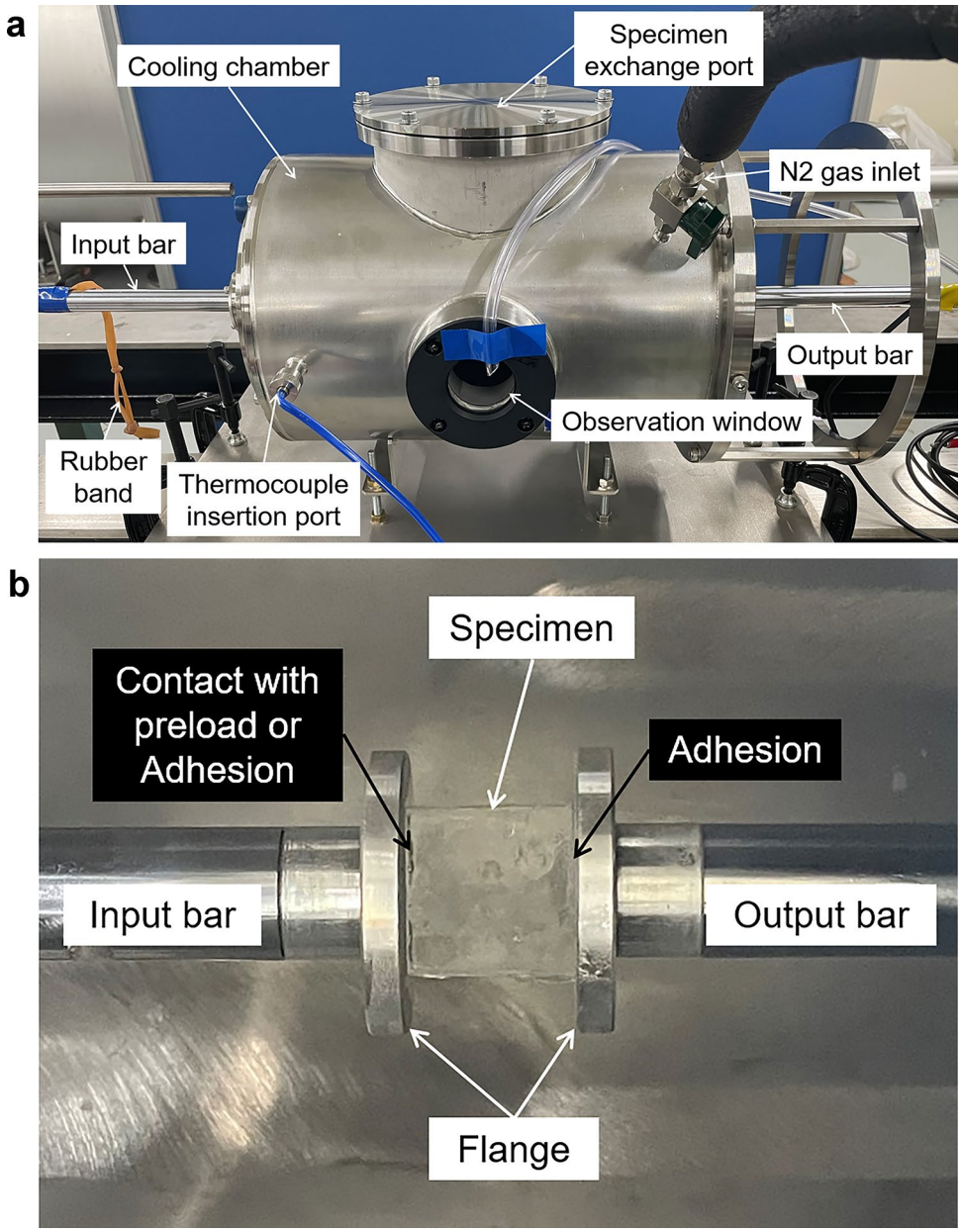

Fig. 2 (**a**) Cooling chamber combined with the split Hopkinson pressure bar testing apparatus. (**b**) Installation of an ice specimen

shaper, the rise of the incident wave was steep. Alternatively, the oscillation of strain wave was observed at the rise of the incident wave when the launch pressure was high. Therefore, we used the cardboard piece as the pulse shaper to increase the rise time of the incident wave and suppress the oscillation of the strain wave in the present study.

To further verify the effect of the pulse shaper, we conducted the SHPB test at room temperature on a 20 mm×20 mm×10 mm specimen made of commercially available acrylonitrile butadiene styrene resin. The stresses on the input and output bar sides were calculated as, respectively, σ_1 and σ_2 by using equations (4) and (7). Figure 4 illustrates the stress–time relationships obtained with and without the pulse shaper. When the pulse shaper was not used, both σ_1 and σ_2 oscillations were observed from the beginning of deformation to ~ 200 μs; this was due to the vibration of the flanges. This stress oscillation was greatly reduced when using the pulse shaper. However, σ_1 did not pass through the origin, and was negative until ~ 20 μs after the beginning of deformation with and without the pulse shaper; this was probably due to the interference of the reflected wave, but it was negligible compared to the measurement time. The rapid increase in σ_1 from ~ 300 μs after the deformation onset was attributed to the influence of the reflected wave, but this did not affect our measurements because the ice specimens fractured in a shorter time, as described later. These results indicate that the SHPB test with flanges was effective in improving the measurement

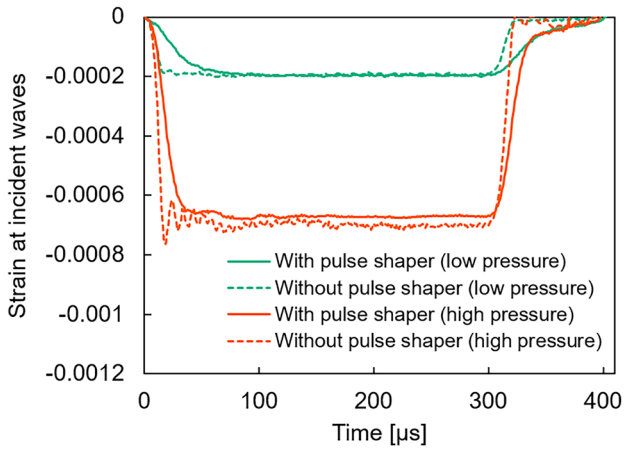

Fig. 3 Strain at incident waves obtained in the split Hopkinson pressure bar test with and without using a pulse shaper

sensitivity for the elastic stress waves, although some waveforms were disturbed even when using the pulse shaper. Hence, we used the pulse shaper in all our experiments.

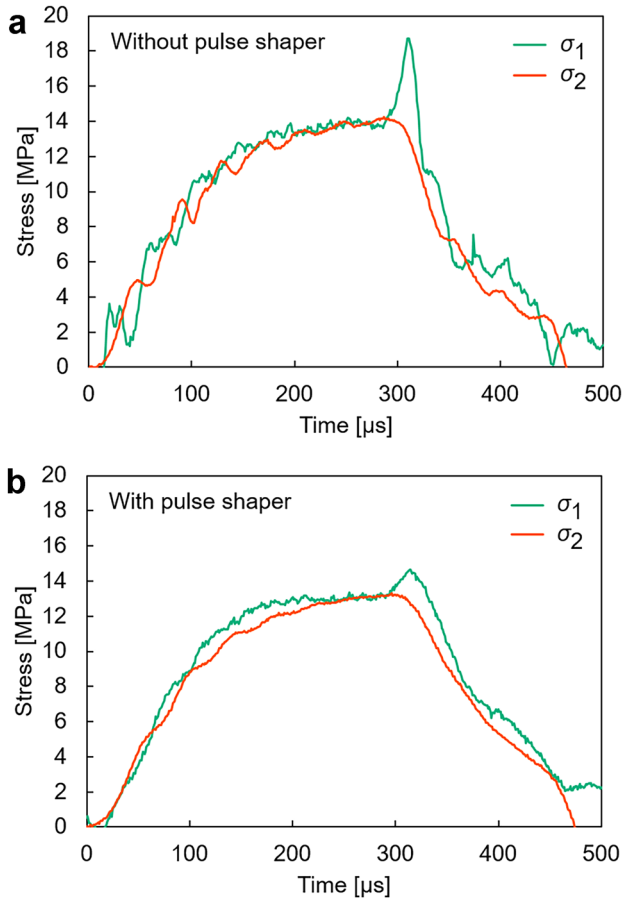

Fig. 4 Stress–time relationships for an acrylonitrile butadiene styrene resin specimen obtained via split Hopkinson pressure bar tests (**a**) without and (**b**) with a pulse shaper

Temperature control

Since we could not measure the temperature of the ice specimens for each experiment, the temperature was preliminarily measured in the cooling chamber. Two K-type thermocouples were used: one was installed inside the chamber and the other was inserted ~ 5 mm inside a 20-mm cube of ice specimen. Nitrogen gas was flowed into the chamber to cool it down, and the chamber space temperature was maintained at approximately – 10 °C to measure the variation of the ice specimen temperature.

Figure 5 compares the variation in the temperature of the chamber space and ice specimen, showing that the ice temperature gradually decreased as the chamber one was cooled to around – 10 °C and maintained. Table 2 summarizes the average ice specimen temperature values obtained with six measurements at different times (5, 10, and 15 min) after the space temperature reached – 10 °C. There was great variability among the measurements conducted after 5 min, but the ice temperature became more stable as the temperature holding time increased. Therefore, we decided to maintain the chamber space temperature for 15 min after reaching – 10 °C, and each experiment was conducted at an ice specimen temperature of – 10.1 °C ± 0.3 °C.

Results and Discussion

Stress–Time Relationship and Fracture Observation

In each test, σ_1 and σ_2 were calculated using equations (4) and (7) to confirm the state of dynamic equilibrium. The resulting stress–time relationships are shown in Fig. 6, along with the average nominal stress (σ_A) calculated with equation (1), and Table 3 lists the experimental conditions and results. Figure 7 shows the deformation and fracture of the

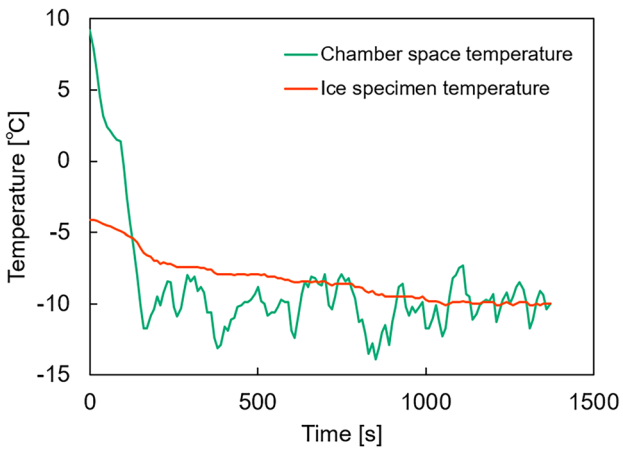

Fig. 5 Temperature variations while cooling down the chamber space

Table 2 Average ice specimen temperature measured at different times after the cooling chamber reached − 10 °C

	After 5 min	After 10 min	After 15 min
Ice specimen temperature	− 8.6 °C ± 1.1 °C	− 9.3 °C ± 0.8 °C	− 10.1 °C ± 0.3 °C

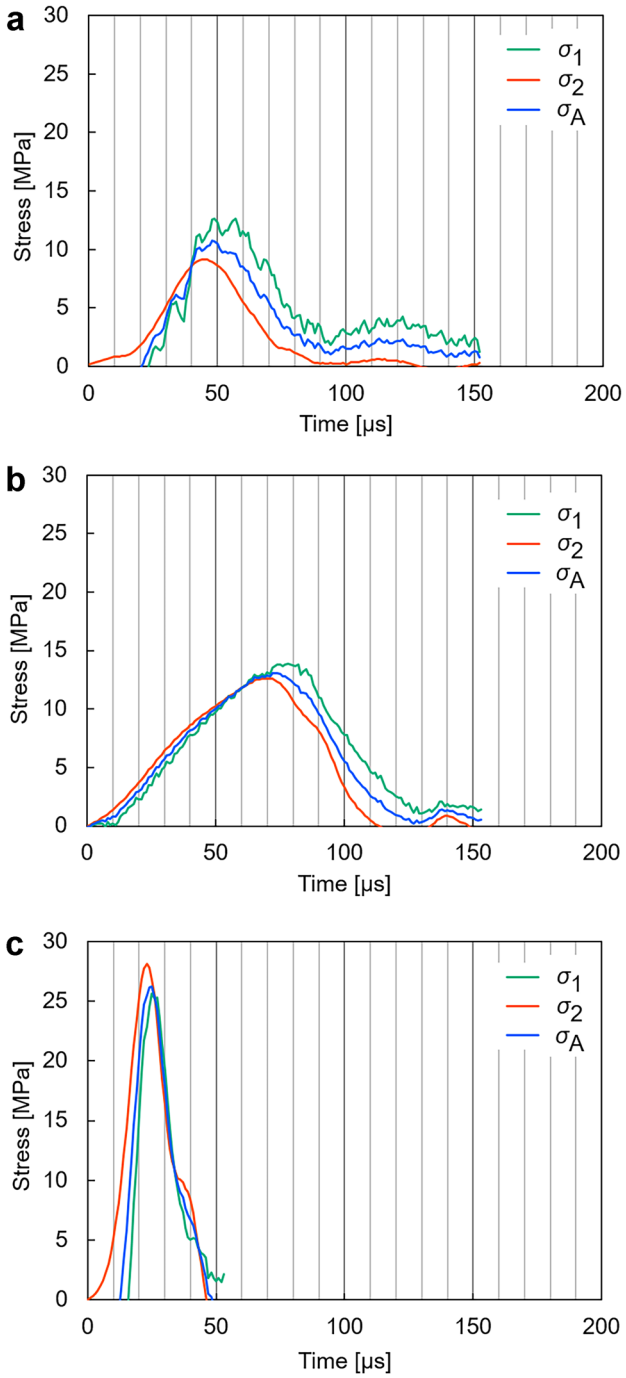

Fig. 6 Stress–time relationship for ice specimens with a length of (**a**) 20, (**b**) 25, and (**c**) 5 mm

ice specimens, as recorded by the high-speed camera, under the experimental conditions. The 20-mm-long specimens (Figs. 6(a) and 7(a)) exhibited a large difference between σ_1 and σ_2 from the initial stage of deformation to the fracture; according to the sequence of photographs taken during this process, the cracks were generated at the input bar side and, then, propagated toward the output bar side only in the upper side of the specimen. A fracture in one direction from the specimen end probably disrupted the axial stress equilibrium, explaining the large stress difference observed between the input and output bars. Meanwhile, the σ_1 of the 25- and 5-mm-long specimens (Fig. 6(b), (c)) was affected by the reflected wave in the initial stage of deformation, which led to a negative output, as mentioned in "Experimental Setup" section. For the 25-mm-long specimens, the effect was almost negligible due to the long deformation time; in contrast, for the 5-mm-long ones, the initial time lag had a relatively large effect due to the short deformation time. However, the difference between σ_1 and σ_2 decreased as the deformation progressed. Therefore, the error rate between the maximum stresses at the input ($\sigma_{1\ max}$) and output sides ($\sigma_{2\ max}$) of these specimens was calculated as`

$$R(\%) = \frac{\sigma_{2max} - \sigma_{1max}}{\sigma_{2max}} \times 100 \tag{11}$$

The R values were relatively consistent with 9.87% and 12.10% for the 25- and 5-mm-long specimens, respectively. However, the R value for the 20-mm-long specimen was 38.15% because of the large stress difference from the initial stage of deformation. Therefore, we defined that the dynamic equilibrium was established when R was within ± 15%, and adopted only the data meeting this condition. The state of dynamic equilibrium was confirmed in 94 out of 173 tests, and these cases were evaluated using the average nominal

Table 3 Experimental conditions and results

Test number	Specimen length (mm)	Air pressure (MPa)	Strain rate at fracture (s^{-1})
25	20	0.188	162
163	25	0.056	9.09
148	5	0.400	551

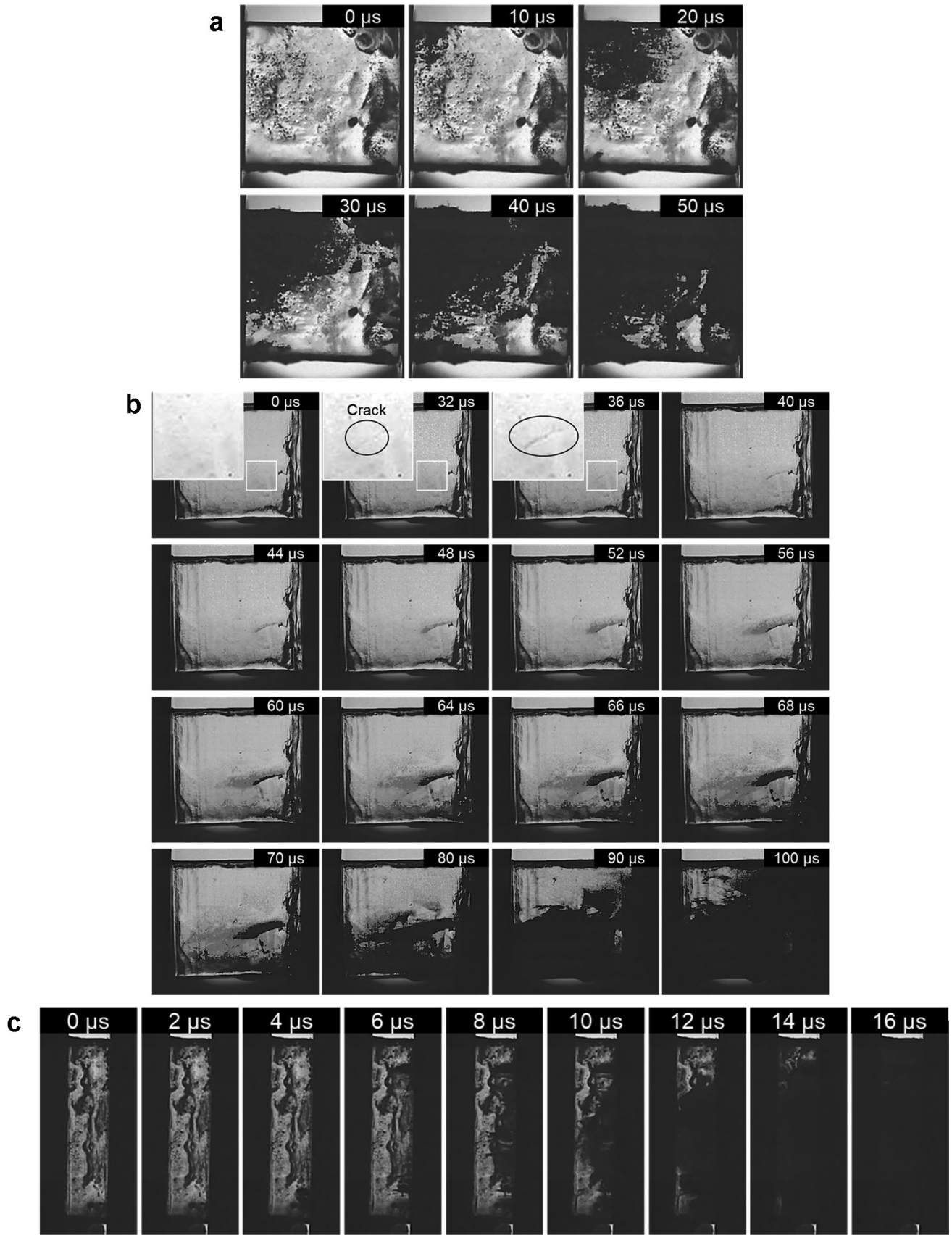
a
0 μs
10 μs
20 μs
30 μs
40 μs
50 μs
b
0 μs
Crack
32 μs
36 μs
40 μs
44 μs
48 μs
52 μs
56 μs
60 μs
64 μs
66 μs
68 μs
70 μs
80 μs
90 μs
100 μs
c
0 μs
2 μs
4 μs
6 μs
8 μs
10 μs
12 μs
14 μs
16 μs

◂**Fig. 7** Images showing the deformation and fracture state of ice specimens with a length of (**a**) 20, (**b**) 25, and (**c**) 5 mm; the top of each image shows the time after the elastic stress wave reached the specimen end facing the input bar side (the left end of the specimen in the images). The black shadows that appear after 0 μs are cracks

stress σ_A in equation (1), although its initial value was missing, as described above. Although the average nominal strain rate and average nominal strain using equations (2) and (3) should be used in this case, this was difficult because of the disturbance of the reflected wave, which we attributed to the flange vibration. In this study, when the dynamic equilibrium could be confirmed, the nominal strain rate and nominal strain were calculated with equations (8) and (9) (i.e., without using the reflected wave), and the results were organized based on them.

Regarding the 25-mm-long specimens, σ_2 increased slowly, reached a peak value around 68–71 μs, and then decreased. When the deformation progressed to ~ 32 μs, a very small crack was observed inside the specimen; afterward, the generated cracks gradually grew and propagated toward both specimen ends (Fig. 7(b)). To understand the relationship between the cracks and the flow stress, we calculated the stress rate ($d\sigma/dt$) and σ_2 was used since σ_A is noisy. Figure 8 shows the relationship between time and the stress or stress rate on the output bar side. For the 25-mm-long specimens, the stress rate increased up to ~ 24 μs and then decreased; however, the crack became visible in the camera image only ~ 32 μs. Since the minimum resolution of the camera used in this study is 74 μm, cracks smaller than that cannot be observed. Moreover, there is a limit to the observation from one direction, and some existing cracks might not be identified. Therefore, the formation of microscopic cracks, which could not be observed by the camera, may have led to the decrease observed in the stress rate. Furthermore, the stress rate decreased rapidly after ~ 66 μs, which corresponds roughly to the time when many cracks started to propagate in the axial direction at once. These results indicate a correlation between stress rate variation and crack generation/propagation.

On the other hand, the stress increased rapidly and σ_2 reached its peak at 23 μs in the 5-mm-long specimens. At that time, multiple cracks were observed generating from the output bar side and propagating toward the input bar side, leading to fracture (Fig. 7(c)). According to the camera observation from one direction, the ice specimen appeared to have already fractured with many cracks at ~ 16 μs, but the stress continued to increase after that. We believe that since it remained between the flanges, the ice specimen continued to be loaded by the inertia effect due to the high deformation rate even after it cracked and turned into fragments, maintaining the increasing trend of the stress. Meanwhile, the stress rate started to decrease after 17 μs (Fig. 8(b)), which is

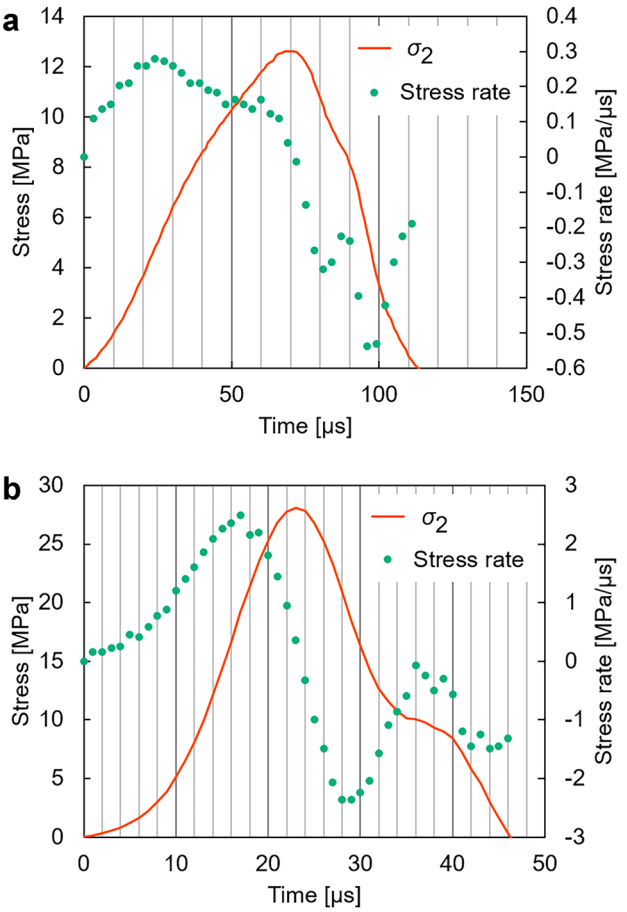

Fig. 8 Stress or stress rate on the output side as functions of time for ice specimens with a length of (**a**) 25 (differentiation at 3-μs intervals) and (**b**) 5 mm (differentiation at 1-μs intervals)

roughly equivalent to the time when the ice appeared to have been fractured by many cracks (Fig. 7(c)). We inferred that the stress rate did not change with the crack generation due to the high deformation rate but the propagation of multiple cracks caused a stress rate change.

Stress–Strain Relationship

Figure 9 displays the stress–strain relationship curves obtained at various strain rates; the experimental conditions and results are summarized in Table 4. The outcomes confirmed that the maximum stress tended to increase along with the strain rate. Besides, after the stress reached its peak value, it gradually decreased, regardless of the strain rate; this tendency has been reported also by Shazly et al. [24, 25] and may be due to the fact that the ice fragments remained constrained between the flanges after the fracture.

As regards the contact condition between specimen and flanges, the stress increased from the initial stage of deformation when the specimens firmly adhered to both flange

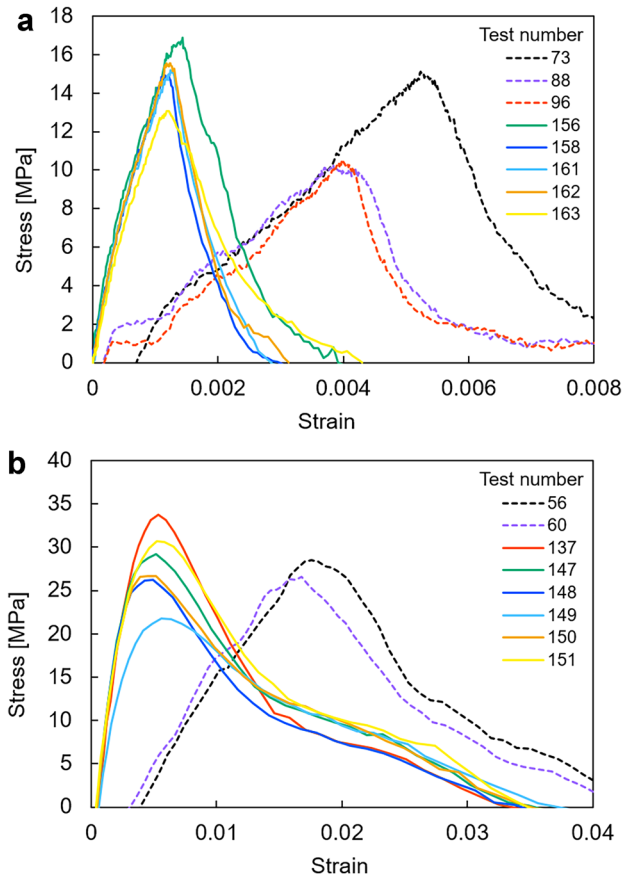

Fig. 9 Stress–strain relationship at strain rates in the ranges of (**a**) 9.09–15.7 and (**b**) 500–706 $s.^{-1}$

ends, while its curve slope was gentle and the strain at the maximum stress was large when the specimens directly adhered to only one flange. This difference arose regardless of the specimen length, and it was probably due to the presence of a small gap between the flange and specimen surfaces before the beginning of deformation, which prevented complete contact. For the 20- and 25-mm-long specimens, the camera images of the test numbers 156, 158, 161, 162, and 163 showed that the cracks generated from inside the specimen (Fig. 7(b)), while those of the test numbers 73, 88, and 96, where only one side adhered to the flange, revealed that the cracks generated and propagated from the unadhered flange side. In contrast, the camera images showed no clear difference in crack generation for the 5-mm-long specimens, regardless of the contact conditions. This happened probably because the difference in stress distribution between specimen edge and center was small due to its short length, and the equilibrium could be maintained even when the cracks were generated from one side; that is, it is synonymous with establishing the dynamic equilibrium by shortening the specimen height in the SHPB method. Hence, these results suggest that the contact condition of the specimen significantly influences the stress–strain relationship in pure ice.

Effect of Specimen Length on the Strain

Here, the results for the specimens adhered to both flange ends are summarized. Figure 10 illustrates the relationship between the strain at the maximum stress and the specimen

Table 4 Experimental conditions and results

Test number	Specimen length (mm)	Contact condition between flanges and specimen	Maximum stress (MPa)	Strain rate at maximum stress (s^{-1})	Strain at maximum stress
73	20	One end adhered (Output bar side)	15.1	14.0	0.00524
88			10.2	13.9	0.00384
96			10.4	13.0	0.00398
156	25	Both ends adhered	16.9	9.30	0.00606
158			14.9	9.59	0.00254
161			15.2	9.50	0.00206
162			15.5	9.09	0.00198
163			13.1	15.7	0.00190
56	5	One end adhered (Output bar side)	28.5	542	0.0175
60			26.6	500	0.0168
137		Both ends adhered	33.7	534	0.00533
147			29.2	608	0.00519
148			26.2	551	0.00495
149			21.8	706	0.00557
150			26.7	589	0.00449
151			30.7	618	0.00521

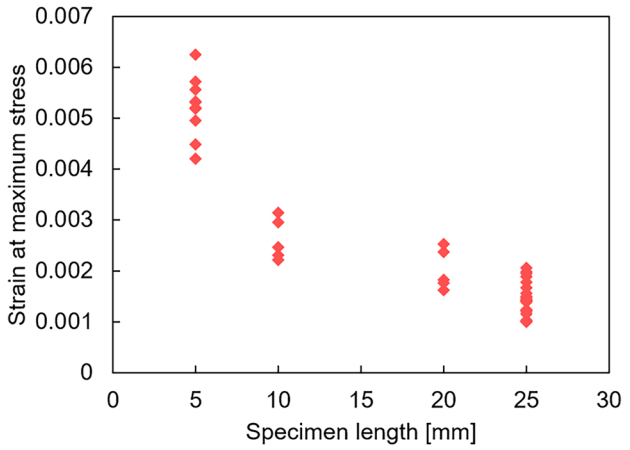

Fig. 10 Relationship between strain at the maximum stress and specimen length

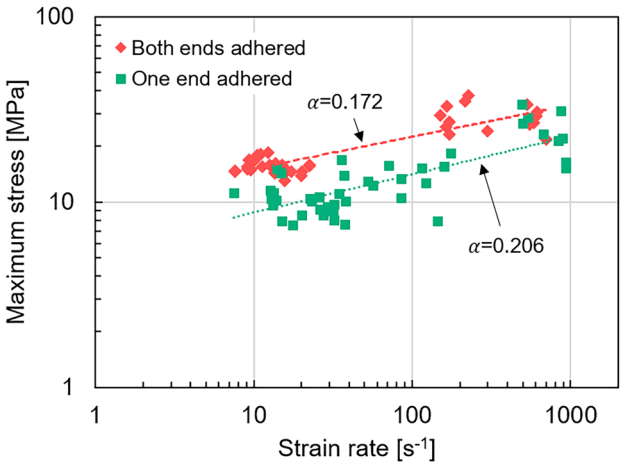

Fig. 11 Relationship between maximum compressive strength and strain rate depending on whether the specimen adhered to one or both flange faces

length, showing a tendency of the strain to increase with decreasing the specimen length. Since the stress–time relationship and camera observation results presented previously indicate that the stress continued to increase even after many cracks appeared in the shorter specimens, we can assume that the strain at the maximum stress also increased when the specimen length was small. In our experiment, we expected that the ice fractured when the maximum stress was reached, as reported in previous studies, but our results suggested that it might have actually fractured before that, demonstrating that the fracture strain of ice at high strain rates cannot be defined only by the stress–strain relationship and a simultaneous camera observation is required. However, since the conclusion that the ice specimens had fractured was based on observations from a single angle, further studies including multidirectional observations are needed to evaluate cracks in the entire ice specimen where the fracture strain can be defined.

Effect of Contact Conditions

Figure 11 displays the relationship between maximum stress and strain rate. The maximum stress of the specimens with both ends adhered to the flanges was higher than those with only one end adhered, indicating that the contact conditions at both specimen ends affect the fracture of ice. As previously mentioned, the specimens with only one end adhered may have cracked from one side, decreasing the maximum stress, due to poor contact between the flange face and specimen. Thus, to measure the compressive stress with the SHPB method, attention must be paid to the contact condition between specimen and testing apparatus so that cracks do not generate from the specimen's end face. On the other hand, Shazly et al. [24, 25] denied the effect of the specimen edge constraint by the jig at high strain rates; they described the friction effect by comparing the use of grease with that of a thin water layer on the contact surface for adhesion. If no grease is applied to the contact surface, cracks will appear from there, while its application may eliminate the unevenness of the ice surface and prevent the cracking from the specimen edges. Therefore, these were likely to be the apparent same conditions as when the specimen adhered to the input and output bars in the present study. We can infer that the results of these two experimental setups by Shazly et al. [24, 25] did not significantly differ since they both prevented the crack generation from the specimen's end face.

The rate of increase in maximum stress along with the strain rate (α) was simply calculated as follows:

$$\sigma = C\dot{\varepsilon}^{\alpha} \tag{12}$$

where C is a constant and α is expressed as the slope of a double-logarithmic plot. The calculated results are shown in Fig. 11. The specimens with only one side adhered to the flange exhibited larger α values, and the difference in maximum stress depending on the contact condition decreased as the strain rate increased. Since the specimens were thin and there was no difference in crack generation/propagation due to different contact conditions in the tests at strain rates above 10^2 s^{-1}, the effect of the initial crack on the maximum stress might have been reduced. Although the specimen thickness was varied to control the strain rate, it was not possible to accurately test all the impact strain rates by using the same specimen thickness and the current equipment. It is a future task to investigate the effect of the specimen thickness, including the experimental method, on ice fracture.

Comparison with Previous Studies

The present study confirmed a positive strain rate dependence of the maximum stress in the strain rate range of approximately 10^1–10^3 s^{-1}. This trend is consistent with the results reported by Kim and Keune [23], Shazly et al. [24, 25], and Song et al. [28], but not with those observed by Dutta et al. [21, 22]. Since the length of the specimens used by the latter was 76.2 mm, perhaps the dynamic equilibrium might have not been established. However, a clear judgment cannot be made because the measurement data by Dutta et al. [21, 22] were not described. The maximum stress results obtained in the present study for the specimens adhered to only one flange side are in good agreement with those reported by Kim and Keune [23] and Shazly et al. [24, 25], while the stress values for the specimens adhered to both flange ends are slightly higher than theirs. There are several possible reasons for this. First, Kim and Keune [23] conducted the experiments at 0 °C and, since the maximum compressive stress of ice increases with decreasing the testing temperature [12–14], our experiments performed at − 10 °C provided higher stress values. Moreover, since their experiments were conducted by cooling the bars with ice bags in a room temperature environment, the melting of the ice on the contact surface might have affected their results. On the other hand, the experiments of Shazly et al. [24, 25] were performed at − 10 °C, the same experimental conditions as in this study; however, the specimen center surface had an interface formed during their specimen preparation process, and this might have reduced the ice maximum compressive stress.

Strain Rate Dependence of Maximum and Fracture Stress

Figure 12(a) compares the results of the present study and our previous quasi-static tests [31] about the relationship between maximum stress and strain rate of ice; the data at the strain rate of 0.8 s^{-1} were newly added in this work. In the previous tests [31], the maximum stress reached a peak value around a strain rate of 10^{-3} s^{-1} and then decreased. These tests were performed using a universal testing machine (5982, Instron), and the specimens adhered to the fixed lower jig but not to the movable upper jig before beginning the measurements. Since ice shows ductile behavior at low strain rates, the effect of this contact condition should be negligible, while it is expected to have a significant effect at strain rates above 10^{-3} s^{-1} because ice begins to exhibit brittle behavior in that condition. This is probably why the results obtained in these previous tests at a strain rate of 10^0 s^{-1} and those observed in the present study with the specimens having only one side adhered to the flange could be expressed by the power approximation represented by

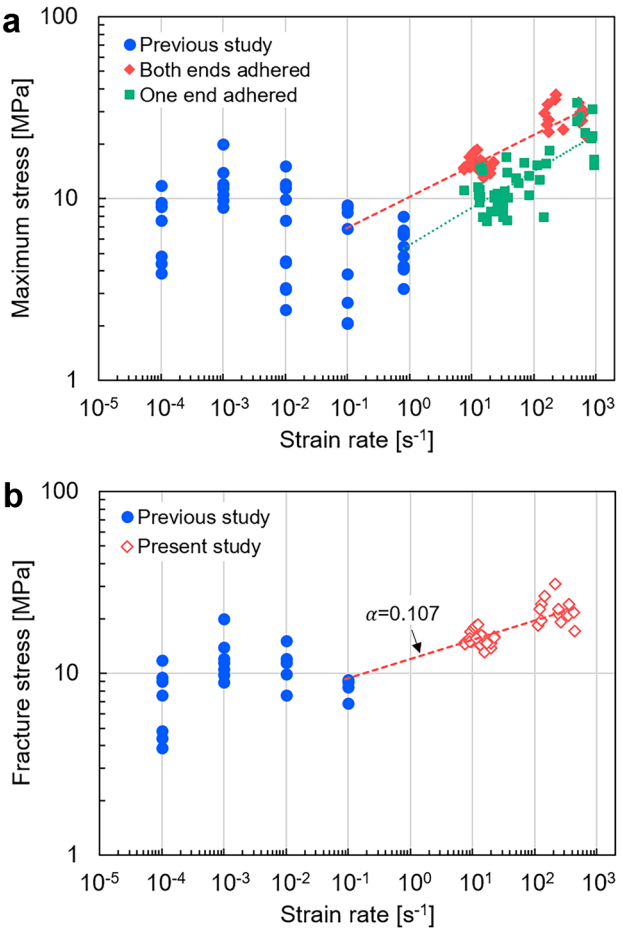

Fig. 12 Comparison of the results of the present study with those of previous tests [31]: (**a**) relationship between maximum stress and strain rate; (**b**) relationship between fracture stress and strain rate

the green dotted line in Fig. 12(a). On the other hand, in our previous indentation tests with spherical indenters, the maximum load, which is the load at the time of ice fracture, decreased when increasing the strain rate from 10^{-3} to 10^{-1} s^{-1} [31]; this trend is similar to that of the maximum stress in the same strain rate range observed in the uniaxial compression tests. The specimens are supposed to have small flaws on the surface due to the cutting process during specimen preparation. Therefore, perhaps only one part of the specimen contacted the jig first, resulting in a complex deformation distribution inside the specimen, similarly to the indentation test. This might have caused stress concentration on the specimen surface, making it more susceptible to cracking from the surface; thus, decreasing the maximum stress in the uniaxial compression test. The power approximation for the specimens with both ends adhered to the flanges, which is represented by the broken, red line in Fig. 12(a), does not pass through the results for a strain rate of 10^0 s^{-1} and overlaps the upper limit of the results for a

strain rate of 10^{-1} s^{-1}. Therefore, in the results of the uniaxial compression tests at strain rates from 10^{-2} s^{-1} to 10^{0} s^{-1}, the specimens with lower maximum stress than the broken, red line of Fig. 12(a) had poor contact conditions and were fractured from the surface as in the indentation test. This suggests that the rate of maximum stress reduction above a strain rate of 10^{-3} s^{-1} was not as large as that observed in our previous study [31] and the ice maximum stress tends to increase at least at a strain rate of $> 10^{-1}$ s^{-1}.

Furthermore, the maximum stress did not coincide with the fracture observed by the camera at high strain rates ($> 10^{2}$ s^{-1}), as discussed in "Stress–Time Relationship and Fracture Observation" and "Effect of Specimen Length on the Strain" sections. This suggests that the maximum stress does not necessarily correspond to the stress at fracture. Therefore, we defined the fracture as the point where the stress rate began to decrease, which roughly corresponded to the time of ice fracture detected via camera observations, at strain rates above 10^{2} s^{-1}. Moreover, we attempted to use the stress at fracture as the fracture stress. However, the dynamic equilibrium was not established because the reflected wave still had a large influence when the stress rate reached the inflection point. For this reason, the fracture stress was summarized using the σ_A values at low strain rates ($\sim 10^{1}$ s^{-1}), where the dynamic equilibrium was established, but using the σ_2 values at high strain rates ($> 10^{2}$ s^{-1}). The strain rate was calculated again with respect to the time of fracture. We deleted the results with stresses lower than the broken, red line in Fig. 12(a), i.e., the results that were obtained at 10^{0} s^{-1} and those measured at 10^{-2}–10^{-1} s^{-1} with lower maximum stresses, because the corresponding specimens were most likely to fracture due to crack generation from the surface.

Figure 12(b) shows the relationship between fracture stress and strain rate. The fracture stress was slightly lower than the maximum stress. Its increase rate, α, at strain rates $> 10^{1}$ s^{-1}, calculated with Eq. (12), was 0.107, which is smaller than the maximum stress one. Furthermore, when compared with Fig. 12(a), the power approximation of the fracture stress was closer to the upper limit of the maximum stress at a strain rate of 10^{-1} s^{-1}. The fracture stress results also suggest that the maximum stress tended to increase at least from a strain rate around 10^{-1} s^{-1}. On the other hand, maximum stress increase at the impact strain rate has been reported in several studies [23–27], but there is no unified view about at what strain rate it begins.

Our maximum and fracture stress results when both specimen ends adhered to the flanges are consistent with those reported by Jones [20]; however, they indicate that the maximum stress of ice at high strain rates does not match the fracture stress. Therefore, to discuss the strain rate dependence of the fracture stress of the ice, SHPB testing method must be combined with high-speed camera observations to correctly evaluate the timing of fracture.

Conclusions

We investigated the measurement of ice compressive stress by reviewing the previous studies that uses the SHPB method. Therefore, we conducted SHPB compression tests with flanged bars on pure ice specimens at − 10 °C while simultaneously observing their internal deformation and fracture state by using a high-speed camera; the contact conditions between the input and output bars and the specimen were also investigated. The dynamic equilibrium was confirmed in each test. When the stress difference between both ends of the specimen was within ± 15%, the dynamic equilibrium was considered as established, and the results were analyzed.

In the specimens with both ends adhered to the flanges, the cracks generated from inside the specimen and propagated when its length was long enough (20 or 25 mm), and the stress rate changed with the crack generation/propagation. In the shorter specimens (5 or 10 mm), instead, the cracks appeared from the edge; moreover, the stress did not decrease when the cracks were generated but continued to increase after the camera observations from one direction detected ice fracture. This suggests that in the shorter specimens the ice might have been already fractured before the stress reached its maximum value. The combination of SHPB testing and camera observation revealed a correlation between crack generation/propagation and stress rate change.

The rate of stress increase with respect to strain was more gradual in the specimens with only one side adhered to the flanges than in those with both ends adhered. Furthermore, the maximum stress remarkably differed between these two specimen groups, and the former showed a lower maximum stress. This was probably due to stress concentration caused by the small gap present between specimen and flange surface in the early stage of deformation, from which the cracks were generated. These results suggest that close attention should be paid to the relationship between the contact conditions of the specimen and the ice maximum stress.

The maximum stress of ice in a strain rate range of 10^{1}–10^{3} s^{-1} exhibited a positive strain rate dependence. The fracture stress, which was redefined as the inflection point of the stress rate at high strain rates ($> 10^{2}$ s^{-1}), was lower than the maximum stress. The results of the impact tests on the specimens with both ends adhered to the flanges and those of our previous quasi-static tests suggest that the maximum and fracture stresses tend to increase at least at a strain rate of $\sim 10^{-1}$ s^{-1}.

These experimental results demonstrate that the establishment of the dynamic equilibrium and the contact condition between specimen and testing apparatus are important aspects for the application of the SHPB compression test to ice. We also showed that fracture of ice at high strain rates cannot be defined with the impact compression test alone but needs high-speed camera observations.

Funding This study was supported by JSPS KAKENHI Grant Number JP17H03152.

Declarations

Conflict of Interests The authors have no competing interests to declare that are relevant to the content of this article.

References

1. Hopkinson B (1914) A method of measuring the pressure in the deformation of high explosives by the impact of bullets. Phil Trans Roy Soc A 213:437–452
2. Kolsky H (1949) An investigation of the mechanical properties of materials at very high rates of loading. Proc Phys Soc B 62:676–700
3. Kolsky H (1963) Stress waves in solids. Dover Publications, New York
4. Chiddister JL, Malvern LE (1963) Compression-impact testing of aluminum at elevated temperatures. Exp Mech 3:81–90. https://doi.org/10.1007/BF02325890
5. Chen W, Song B, Frew DJ, Forrestal MJ (2003) Dynamic small strain measurements of a metal specimen with a split Hopkinson pressure bar. Exp Mech 43:20–23. https://doi.org/10.1007/BF02410479
6. Daniel IM, Cho JM (2011) Characterization of anisotropic polymeric foam under static and dynamic loading. Exp Mech 51:1395–1403. https://doi.org/10.1007/s11340-011-9466-3
7. Koumilis S, Lamberson L (2019) Strain rate dependent compressive response of open cell polyurethane foam. Exp Mech 59:1087–1103. https://doi.org/10.1007/s11340-019-00521-3
8. Gong JC, Malvern LE, Jenkins DA (1990) Dispersion investigation in the split Hopkinson pressure bar. J Eng Mater Technol 112(3):309–314. https://doi.org/10.1115/1.2903329
9. Frew DJ, Forrestal MJ, Chen W (2002) Pulse shaping techniques for testing brittle materials with a split hopkinson pressure bar. Exp Mech 42:93–106. https://doi.org/10.1007/BF02411056
10. Hawkes I, Mellor M (1972) Deformation and fracture of ice under uniaxial stress. J Glaciol 11(61):103–131. https://doi.org/10.3189/S002214300002253X
11. Gold LW (1977) Engineering properties of fresh-water ice. J Glaciol 19(81):197–212. https://doi.org/10.3189/S0022143000215608
12. Arakawa M, Maeno N (1997) Mechanical strength of polycrystalline ice under uniaxial compression. Cold Reg Sci Technol 26(3):215–229. https://doi.org/10.1016/S0165-232X(97)00018-9
13. Higashi A, Koinuma S, Mae S (1964) Plastic yielding in ice single crystals. Jpn J Appl Phys 3(10):610–616
14. Schulson EM (1990) The brittle compressive fracture of ice. Acta Metall Mater 38(10):1963–1976. https://doi.org/10.1016/0956-7151(90)90308-4
15. Sinha NK (1982) Constant strain-and stress-rate compressive strength of columnar-grained ice. J Mater Sci 17:785–802. https://doi.org/10.1007/BF00540376
16. Mellor M, Cole DM (1982) Deformation and failure of ice under constant stress or constant strain-rate. Cold Reg Sci Technol 5(3):201–219. https://doi.org/10.1016/0165-232X(82)90015-5
17. Schulson EM, Iliescu D, Fortt A (2005) Characterization of ice for return-to-flight of the space shuttle: Part 1 - hard ice. Tech Pep NASA CR-2005–213643-Part 1
18. Schulson EM (2001) Brittle failure of ice. Eng Fract Mech 68:1839–1887. https://doi.org/10.1016/S0013-7944(01)00037-6
19. Cole DM (2001) The microstructure of ice and its influence on mechanical properties. Eng Fract Mech 68(17–18):1797–1822. https://doi.org/10.1016/S0013-7944(01)00031-5
20. Jones SJ (1997) High strain-rate compression test on ice. J Phys Chem B 101(32):6099–6101. https://doi.org/10.1021/jp963162j
21. Dutta PK (1993) Compressive failure of polycrystalline ice under impact. Proc of the Third Intren Offshore Polar Eng Conf 573–580
22. Dutta PK, Cole DM, Schulson EM, Sodhi DS (2004) A fracture study of ice under high strain rate loading. Int J Offshore Polar 14:182–188
23. Kim H, Keune JN (2007) Compressive strength of ice at impact strain rates. J Mater Sci 42:2802–2806. https://doi.org/10.1007/s10853-006-1376-x
24. Shazly M, Prakash V, Lerch BA (2006) High-strain-rate compression testing of ice. Tech Pep NASA TM-2006–213966
25. Shazly M, Prakash V, Lerch BA (2009) High strain-rate behavior of ice under uniaxial compression. Int J Solids Struct 46:1499–1515. https://doi.org/10.1016/j.ijsolstr.2008.11.020
26. Wu X, Prakash V (2015) Dynamic strength of distill water and lake water ice at high strain rates. Int J Impact Eng 76:155–165. https://doi.org/10.1016/j.ijimpeng.2014.09.013
27. Bragov A, Igumnov L, Konstantinov A, Lomunov A, Filippov A, Shmotin Yu, Didenko R, Krundaeva A (2015) Investigation of strength properties of freshwater ice. EPJ Web of Conferences 94:01070. https://doi.org/10.1051/epjconf/20159401070
28. Song Z, Wang Z, Kim H, Ma H (2016) Pulse shaper and dynamic compressive property investigation on ice using a large-sized modified split Hopkinson pressure bar. Lat Am J Solids Struct 13(3):391–406. https://doi.org/10.1590/1679-78252458
29. Potter RS, Cammack JM, Braithwaite CH, Church PD, Walley SM (2019) Problems associated with making mechanical measurements on water–ice at quasistatic and dynamic strain rates. J Dyn Behav Mater 5:198–211. https://doi.org/10.1007/s40870-019-00202-1
30. Sutton MA, Orteu JJ, Schreier H (2009) Image correlation for shape, motion and deformation measurements, basic concepts, theory and applications. Springer Science & Business Media, New York
31. Nakao Y, Yamada H, Ogasawara N, Matsuzawa T (2021) Ductile and brittle behavior during deformation and fracture for pure ice detected by quasi-static indentation test. Mech Eng J 8(3):21–00083. https://doi.org/10.1299/mej.21-00083
32. Tateyama K, Yamada H, Ogasawara N, Okui R, Ogawa K (2015) Dynamic compressive behavior of foamed polyethylene film. EPJ Web Confer 94:01038. https://doi.org/10.1051/epjconf/20159401038
33. Tateyama K, Yamada H, Ogasawara N (2016) Effect of strain rate on compressive properties of foamed polyethylene film. Polym Test 52:54–62. https://doi.org/10.1016/j.polymertesting.2016.04.002